FULL PAPER

3D gradient echo snapshot CEST MRI with low power saturation for human studies at 3T

Anagha Deshmane[1] (iD) | Moritz Zaiss[1] (iD) | Tobias Lindig[2] | Kai Herz[1] |
Mark Schuppert[1] | Chirayu Gandhi[1] | Benjamin Bender[2] | Ulrike Ernemann[2] |
Klaus Scheffler[1,3]

[1]High-field Magnetic Resonance Center, Max Planck Institute for Biological Cybernetics, Tübingen, Germany

[2]Department of Diagnostic and Interventional Neuroradiology, University Clinics Tübingen, Tübingen, Germany

[3]Department of Biomedical Magnetic Resonance, Eberhard-Karls University Tübingen, Tübingen, Germany

Correspondence
Moritz Zaiss, High-field Magnetic Resonance Center, Max Planck Institute for Biological Cybernetics, Max-Planck-Ring 11, 72076 Tübingen, Germany.
Email: moritz.zaiss@tuebingen.mpg.de

Purpose: For clinical implementation, a chemical exchange saturation transfer (CEST) imaging sequence must be fast, with high signal-to-noise ratio (SNR), 3D coverage, and produce robust contrast. However, spectrally selective CEST contrast requires dense sampling of the Z-spectrum, which increases scan duration. This article proposes a compromise: using a 3D snapshot gradient echo (GRE) readout with optimized CEST presaturation, sampling, and postprocessing, highly resolved Z-spectroscopy at 3T is made possible with 3D coverage at almost no extra time cost.

Methods: A 3D snapshot CEST sequence was optimized for low-power CEST MRI at 3T. Pulsed saturation was optimized for saturation power and saturation duration. Spectral sampling and postprocessing (B_0 correction, denoising) was optimized for spectrally selective Lorentzian CEST effect extraction. Reproducibility was demonstrated in 3 healthy volunteers and feasibility was shown in 1 tumor patient.

Results: Low-power saturation was achieved by a train of 80 pulses of duration $t_p = 20$ ms (total saturation time $t_{sat} = 3.2$ seconds at 50% duty cycle) with $B_1 = 0.6$ μT at 54 irradiation frequency offsets. With the 3D snapshot CEST sequence, a $180 \times 220 \times 54$ mm field of view was acquired in 7 seconds per offset. Spectrally selective CEST effects at +3.5 and –3.5 ppm were quantified using multi-Lorentzian fitting. Reproducibility was high with an intersubject coefficient of variation below 10% in CEST contrasts. Amide and nuclear overhauser effect CEST effects showed similar correlations in tumor and necrosis as show in previous ultra-high field work.

Conclusion: A sophisticated CEST tool ready for clinical application was developed and tested for feasibility.

KEYWORDS
APT, brain tumor, chemical exchange saturation transfer, magnetization transfer, NOE

1 | INTRODUCTION

Chemical exchange saturation transfer (CEST) allows for indirect detection of diluted molecules by their saturation transfer to the abundant water pool.[1-3] Many different diluted solutes were reported to be detectable with CEST such as peptides and proteins,[3-6] with dependency on protein conformation,[7-9] creatine,[10,11] glutamate,[12,13] or even injected solutes such as iopamidol,[14-16] glucose,[17-20] and glucose derivatives.[21,22]

Regarding CEST imaging applications, there are usually competing interests of radiologists and medical physicists. Radiologists want reliable image contrasts at clinical field strengths in negligible scan time, with high signal-to-noise ratio (SNR) and 3D coverage. On the other hand, physicists aim to sample the Z-spectrum with high spectral resolution in order to facilitate accurate and reliable fitting of model peaks known to exist from studies at ultra-high field (UHF) strengths. UHF studies at 9.4 and 7T have revealed spectrally selective CEST effects related to proteins, including amide, amine, and nuclear overhauser effect (NOE) effects, as well as smaller peaks potentially related to creatine and choline phospholipids.[10,11,23,24] Moreover, spatial correlations between isolated amide CEST and gadolinium ring enhancement have been reported.[5,6] Changes in NOE were also shown to correlate with histology[25] and be a measure for brain tumor therapy response at 7T.[26] Therefore, there is clinical interest in isolation of spectrally selective CEST effects at lower field strengths.

Because of peak broadening and lower SNR at clinical field strengths, the frequency separation of different CEST effects is difficult. Many previously published applications of CEST evaluate Z-spectrum asymmetry (MTR_{asym}) to identify CEST contrast while removing direct water saturation effects. MTR_{asym} approaches can be performed with a limited number of scans and are therefore relatively fast and can be performed clinically in 3D mode.[27,28] An important measure for CEST sequence efficiency is the acquisition time per irradiation frequency offset, which is currently around 30 seconds per offset for 3D CEST sequences at 3T.[29] Spectrally selective CEST, on the other hand, needs more spectral samples and therefore longer scan time, which is often traded for single-slice measurements with 4 seconds[30] to 11.25 seconds[31] per offset. In this work, we show that a snapshot 3D readout[32] and optimized saturation scheme can be used to obtain CEST contrast with an acquisition time of 7 seconds per irradiation frequency offset. With this more-efficient acquisition, more time can be invested to sample the Z-spectrum finely, allowing for use of more-advanced CEST metrics and resulting in isolated CEST effects at 3T with similar contrast to those previously observed at 9.4T.

At 3T, slow exchanging pools (e.g., NOE and amides) benefit in both spectral selectivity as well as effect strength when going to lower saturation powers. Herein, we analyzed the dependency of CEST effects as a function of saturation power and saturation time with regard to effect strength as well as spectral selectivity. We show that separation of NOE and amide signals is possible and can be robustly mapped using sophisticated postprocessing. Using the snapshot readout revealed that these NOE- and amide-CEST maps can be acquired in 3D without compromising scan time. This capability enables volumetric coverage of lesions and motion correction, which is important for future clinical studies.

2 | METHODS

2.1 | In vivo measurements

Imaging was performed on a 3T whole-body MRI system (MAGNETOM Prisma; Siemens Healthcare, Erlangen, Germany) on 3 healthy volunteers and 1 patient with a brain tumor with informed consent and approval by the local ethics committee. The vendor's Head/Neck 64 coil (64 channels) was used for signal reception.

The CEST sequence consisted of a presaturation module followed by a single-shot radiofrequency (RF) and gradient spoiled gradient-echo readout using centric spiral reordering. The imaging parameters were field of view = $220 \times 180 \times 54$ mm^3 and matrix size $128 \times 104 \times 18$ for $1.7 \times 1.7 \times 3$ mm^3 resolution, thus with acceleration factor $R_y = 2$ and elliptical scanning mode (factor $4/\pi$ more k-space lines) a phase-encoding matrix of 41×18 for a total of 738 acquired k-space lines, TE = 2 ms, TR = 4 ms, bandwidth (BW) = 700 Hz/pixel, 18 slices, (FA) = 6°, and elongation factor E = 0.5 (rectangular spiral according to a previous work[32]). These settings resulted in a readout time of t_{RO} = 738×0.004 seconds = 2.9 seconds.

The spectrally, but not spatially, selective CEST saturation module was optimized experimentally in a healthy volunteer by varying the pulse duration and saturation power for a train of 180° pulses. The optimal saturation period later applied for reproducibility and patient measurements consisted of a train of 80 or 100 Gaussian-shaped RF pulses with pulse time t_{pulse} = 20 ms, interpulse delay t_{delay} = 20 ms, resulting in total saturation time t_{sat} = 3.2 to 4 seconds, and $B_{1,mean}$ = 0.6 µT. After the pulse train, a crusher gradient was applied to destroy spurious transversal magnetization before the next saturation block. Z-spectrum data were obtained after saturation at 54 irradiation frequency offsets: –300 ppm for an unsaturated reference image, ±100 ppm, ±50 to ±20 ppm in steps of 10 ppm, ±10 to ±1 ppm in steps of 0.5 ppm, and –0.5 to 0.5 ppm in steps of 0.25 ppm. A similar saturation module was used previously at 7T with a single-slice readout.[5,6,33] Acquisition time per offset was TA = t_{sat} + t_{RO} = 6.1 to 6.9 seconds. For 54 irradiation frequency offsets, plus acquisition of the generalized autocalibrating partially parallel

acquisition (GRAPPA) calibration kernel (32 × 18 lines) followed by 12-second recovery time before the first CEST module, this yielded a total scan time of approximately 5.8 to 6.5 minutes for the total high-resolution CEST-spectrum scan. For validation of CEST contrasts found at 3T, 1 subject was additionally scanned with a similar low-power Z-spectrum protocol previously optimized at 9.4T.[23,34]

Images were reconstructed offline using a $\sqrt{2}$ k-space filter and adaptive coil combination.[35] Reconstructed 4D data sets were motion corrected using the AFNI 3Dvolreg function.[36]

2.2 | Data evaluation

CEST images were generated from the Z-value that is given by the fraction of the saturated image S_{sat} and the fully relaxed image S_0 (Equation 1):

$$Z(\Delta\omega) = \frac{S_{sat}(\Delta\omega)}{S_0} \quad (1)$$

Spectrally selective CEST effects were evaluated using Lorentzian line fitting in a 4-step process:

1. 2-pool Lorentzian fitting for B_0 determination
2. B_0 correction and denoising of data
3. 2-pool Lorentzian fitting on B_0 corrected data, generation of MTR_{LD}
4. 3-pool Lorentzian fitting of MTR_{LD} for isolated CEST contrast

In step 1, a 2-pool model was used to describe the background signals direct water saturation and semisolid magnetization transfer (ssMT). Only irradiation frequency offsets assumed to be effected solely by the background signal were used for the fit (ssMT: ±100, ±50, ±40, ±30, ±20, -10, ±9.5, -9, ±8.5, $+7.5$, and $+6.5$ ppm; water: ±1, ±0.5, ±0.25, and 0 ppm); interleaved sampling allowed for more-stable simultaneous fitting of ssMT and broadened CEST effects in the 3T spectrum. Other irradiation frequency offsets were excluded. The utilized 2-pool fit model is given by the direct water saturation (w) and ssMT (Equation 2):

$$Z(\Delta\omega) = c - L_w - L_{ssMT} \quad (2)$$

with a constant c and the adjusted Lorentzian L_w of the water line. L_w includes a plateau to account for the pulse bandwidth at 3T defined by Equation 3:

$$L_w = A_w \frac{\Gamma_w^2/4}{\Gamma_w^2/4 + (x \bullet \Theta[x] + y \bullet \Theta[-y])^2} \quad (3)$$

where A is the Lorentzian amplitude, Γ is the Lorentzian width, and δ is the center frequency. Here, $\Theta[\bullet]$ is the Heaviside

function with $x = \left(\Delta\omega - \delta_w - \frac{BW}{2}\right)$ and $y = \left(\Delta\omega - \delta_w + \frac{BW}{2}\right)$. The parameter BW accounts for the width of the plateau and is an estimation of the Fourier width of the Gaussian saturation pulse and was kept constant at $BW = 1/(t_{pulse}\frac{\gamma}{2\pi}B_0)$. The second pool representing ssMT is a Lorentzian function defined by Equation 4:

$$L_{ssMT} = A_{ssMT} \frac{\Gamma_{ssMT}^2/4}{\Gamma_{ssMT}^2/4 + (\Delta\omega - \delta_{ssMT})^2} \quad (4)$$

The Lorentzian ssMT pool was allowed to be centered off-resonant between 0 and –2.5 ppm. Although super-Lorentzian line shapes were also investigated for ssMT fitting (see Supporting Information), the proposed Lorentzian line shapes were found to be sufficient and robust. Note that only symmetric super-Lorentzian line shapes were investigated because of ambiguity in modeling and interpolation in simulated low-power line shapes (see Supporting Information Figure S6).

In step 2, the off-resonance of the water pool in the initial 2-pool model was used as a surrogate B_0 map, and Z-spectra were shifted to correct for field shifts. These B_0-corrected Z-spectra were then spectrally denoised using principal component analysis (PCA), retaining 9 of 53 components (details provided in Supporting Information Figures S7–S10).

For peak-selective CEST evaluation, the Lorentzian difference method was used according to a previous work[5] (Equation 5):

$$MTR_{LD} = Z_{fit,ref} - Z \quad (5)$$

Here, $Z_{fit,ref}$ is the 2-pool background fit, which was repeated on the B_0-corrected and denoised Z-spectra in step 3.

Finally, in step 4, a 3-pool Lorentzian model was used to fit the MTR_{LD} spectrum at offsets $+10$, $+9$, ±8, -7.5, ±7, -6.5, ±6, ±5.5, ±5, ±4.5, ±4.0, ±3.5, ±3.0, ±2.5, ±2.0, and ±1.5 ppm (those previously excluded from the background fit) to isolate the amide ($+3.5$ ppm), amine ($+2.0$ ppm), and NOE (-3.5 ppm) resonances (Equation 6):

$$MTR_{LD}(\Delta\omega) = c + L_{+2ppm} + L_{+3.5ppm} + L_{-3.5ppm} \quad (6)$$

and (Equation 7)

$$L_x = A_x \frac{\Gamma_x^2/4}{\Gamma_x^2/4 + (\Delta\omega - \delta_x)^2} \quad (7)$$

All pool-fitting parameters can be found in Supporting Information Tables S3 to S6. Quantitative maps were generated from the fitting parameter A_x for the three CEST pools and the ssMT pool. All multi-Lorentzian fitting was

performed in MATLAB (The Mathworks, Inc., Natick, MA); code is available online at www.cest-sources.org. The total postprocessing time, including B_0 estimation and correction, denoising, background signal removal, and CEST pool fitting on each 4D stack, was approximately 7.5 minutes using parallel computation on a 12-core, 2.2-GHz computer.

Region of interest (ROI) analysis of CEST effects was performed in gray and white matter segments of a single slice in each subject. Tissue segments were approximated by thresholding the ssMT pool map. Slices for tissue analysis were chosen to ensure similar tissue distributions in each subject. Coefficient of variation across subjects (standard deviation divided by the mean) was used to determine reproducibility of fitted pool sizes.

3 | RESULTS

3.1 | Contrast and imaging optimization

Optimal B_1 saturation power was determined by repeating measurements in a healthy subject at different B_1 levels. Figure 1 shows representative B_0-corrected Z-spectra and MTR_{LD} spectra in gray and white matter ROIs for different B_1 power levels. As B_1 was increased from 0.3 µT to 0.8 µT, saturation at +3.5, +2.0, and −3.5 ppm increased, as did the broader background signal (Figure 1A,B). Removal of the direct water and ssMT contributions (Figure 1C,D) revealed increasing CEST effects with increased B_1 power, which were spectrally selective at +3.5, +2.0, and −3.5 ppm. However, gray matter/white matter contrast (Figure 1E) at the +3.5-, +2.0-, and −3.5-ppm resonances was optimized for B_1 =
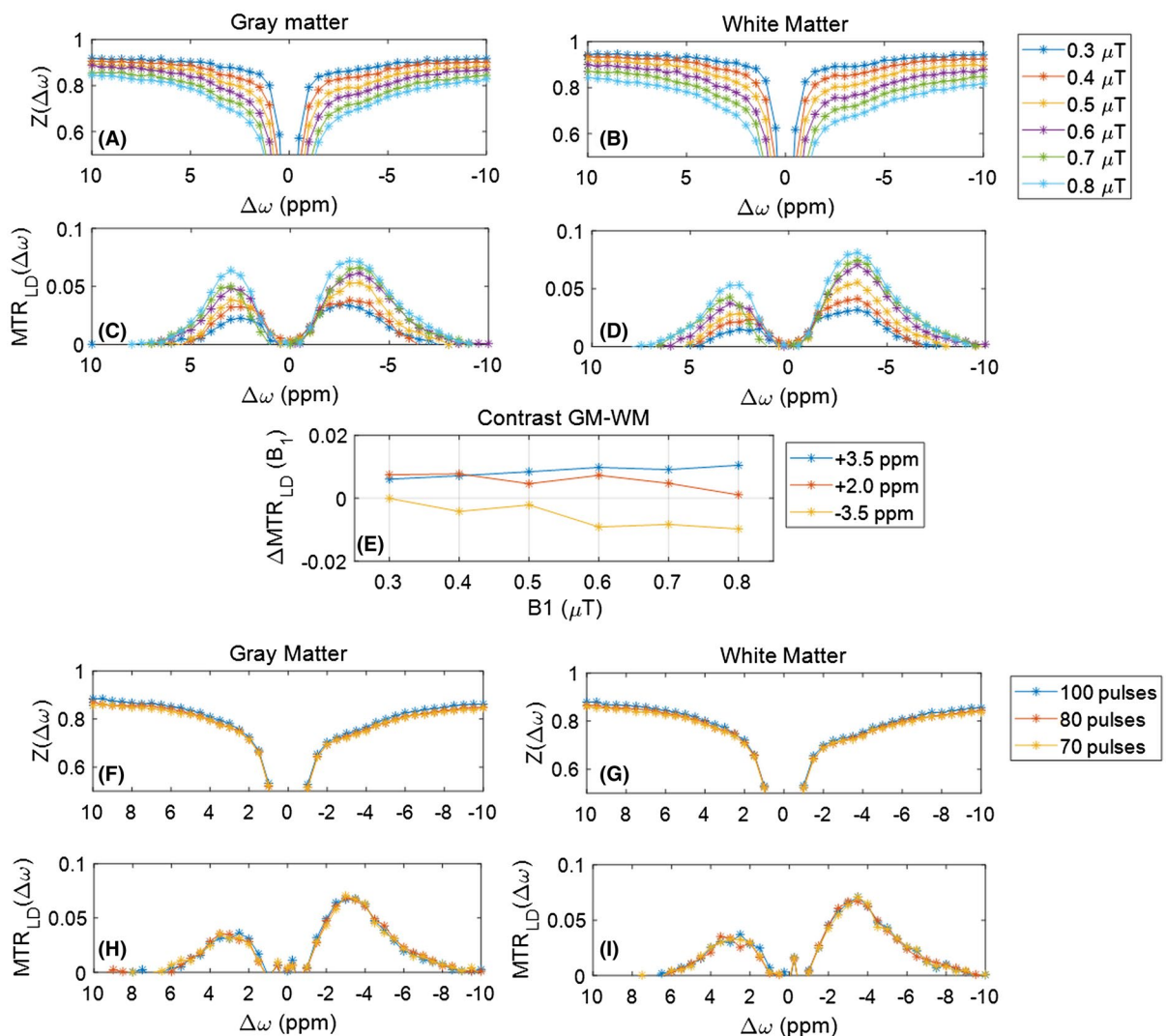
FIGURE 1 Contrast optimization. B_1 dispersion of Z-spectra (A,B) and MTR_{LD} effects (C,D) in gray matter (GM) and white matter (WM) show that higher power with shorter pulses broadens the CEST peaks. Spectrally selective CEST effects are maximized at 0.8 µT, whereas GM-WM contrast at +3.5, +2, and −3.5 ppm is maximized at 0.6 to 0.7 µT (E). The dependency of Z-spectra (F,G) and CEST effects (H,I) on total saturation time is negligible. The same saturation and contrast can be sufficiently achieved with shorter saturation time, improving clinical feasibility. Z-spectra and MTR_{LD} spectra are in arbitrary units

0.6 µT. The $B_1 = 0.6$ µT power was also consistent with the 180° pulse shown previously to be most efficient.[37] Figure 1F–I shows that the spectrally selective CEST contrast with $B_1 = 0.6$ µT was maintained using a saturation train of 100, 80, and 70 Gaussian pulses at 50% duty cycle ($t_{sat} = 4$, 3.2, and 2.8 seconds, respectively), improving clinical feasibility with shorter scan time.

3.2 | CEST contrasts

Background fitting, shown in Figure 2, was achieved in a stable 2-pool fit. The addition of the BW parameter in the direct water saturation allowed for good approximation of the width of the water peak (Figure 2B,C), and far off-resonant points enabled stable fitting of the ssMT pool (Figure 2A,D). More information on the background fit optimization can be found in Supporting Information Figures S1–S6.

The residual between the background fit (red line in Figure 2) and the measured Z-spectra data, also referred to as the Lorentzian difference spectrum or MTR_{LD}, revealed spectrally selective CEST effects shown in Figure 3. Lorentzian difference images at individual irradiation frequency offsets already revealed clear gray/white matter contrast at the +3.5- and −3.5-ppm resonances. Whereas the MTR_{LD} at +2.0 ppm appeared slightly increased in gray matter compared to white matter, anatomical structure was not immediately discernable and values in ROIs were not statistically significant (see Figure 3D).

The result of fitting the MTR_{LD} spectrum with 3 Lorentzian pools is shown in 3 volunteers in Figure 4A–C. Whole-brain images are provided in Supporting Information Figure S12. Fitted CEST effects at +3.5 and −3.5 ppm followed the

expected contrast distribution in gray and white matter. The fitted +2.0-ppm CEST contrast was heavily influenced by direct water saturation. Additionally, residual off-resonance effects from the background signal removal procedure obscured the contrast between gray and white matter. Figure 4D–F shows that mean MTR_{LD} spectra in gray and white matter segments in 3 healthy subjects were in good agreement. Coefficient of variation across subjects was less than 10% for fitted +3.5-ppm, −3.5-ppm, and ssMT pool sizes in both gray and white matter, indicating good reproducibility of these effects. However, coefficient of variation of the fitted +2.0-ppm resonance amplitude was 68% in gray matter and 60% in white matter.

An additional scan at 9.4T was performed for 1 subject with a similar saturation scheme.[23] This allowed for direct validation of 3T spectrally selective CEST contrasts. Figure 5 shows that although 3T CEST effects were small, broad, and coalesced, the fitted contrasts at +3.5 ppm, −3.5 ppm, and ssMT were similar using the optimized 3T protocol to those found at 9.4T. Whereas UHF strength provides higher SNR, the use of spectral denoising on the highly sampled 3T data allowed for comparable anatomical detail in these contrasts. However, the slight gray/white matter contrast visible in the +2.0-ppm resonance at 9.4T could not be replicated at 3T using the current saturation scheme and postprocessing.

3.3 | Tumor patient

Fitted CEST contrasts in a brain tumor patient are shown in Figure 6. Gray matter/white matter contrasts were similar in the ssMT, +3.5-ppm, and −3.5-ppm pools as in the healthy subjects. Similar to previous findings at UHF, the isolated
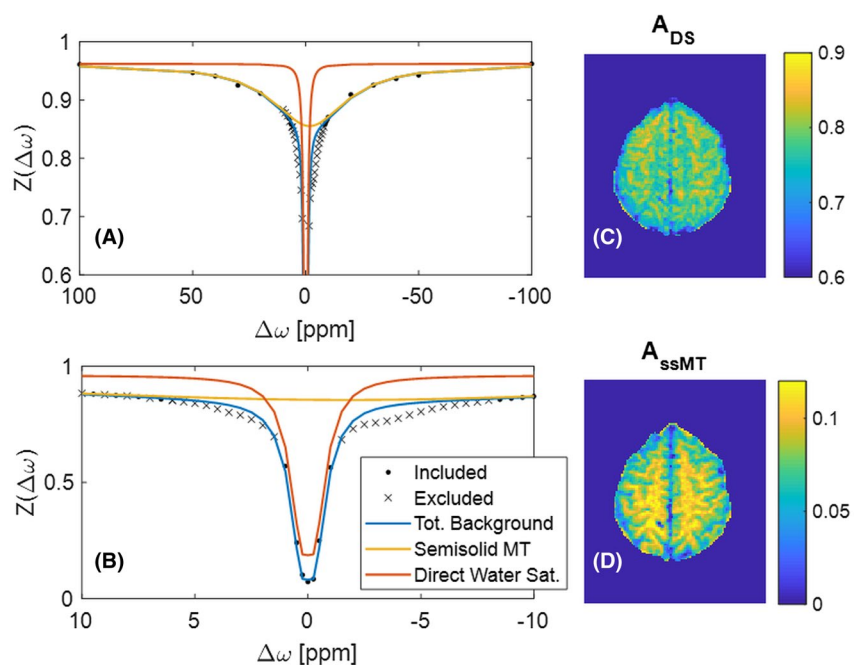
FIGURE 2 Background signal fitting. (A,B) The total background signal (blue), with contributions from direct water saturation (DS; orange) and the ssMT pool (yellow), is fitted according to Equations –4. Points between ±0.5 and ±10 ppm where CEST effects are expected to occur (crosses) were excluded from the background fit. (C,D) Fitted DS and ssMT pool amplitudes in arbitrary units
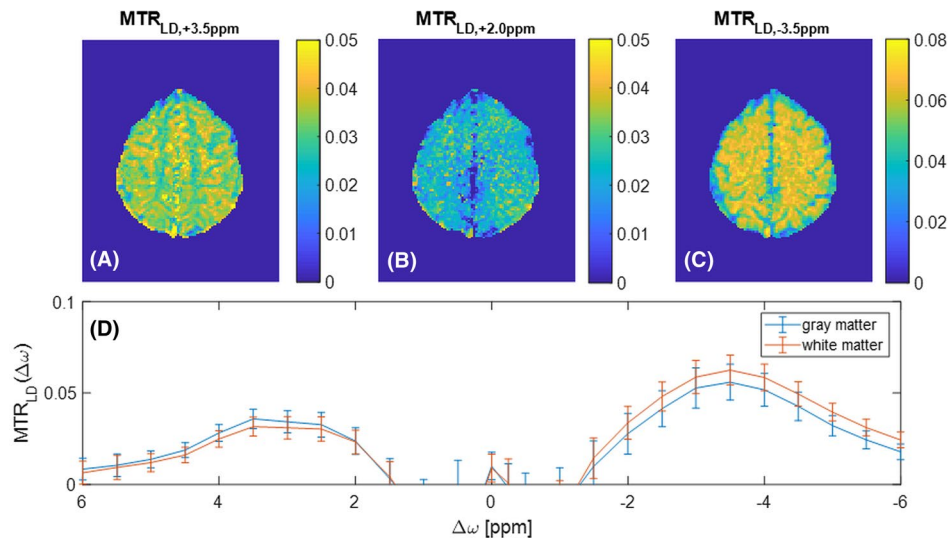
FIGURE 3 CEST effect fitting of Lorentzian difference spectrum (MTR$_{LD}$). The Lorentzian difference signal (Equation 5) reveals CEST contrasts at individual offsets (A–C) and in the MTR$_{LD}$ spectrum in gray and white matter segments in a single slice (D). Error bars represent standard deviation across gray and white matter voxels, respectively, in a single subject. MTR$_{LD}$ is expressed in arbitrary units

3T CEST effects showed some correlations between the amide signal and the gadolinium ring enhancement and depleted NOE signals in the tumor area and especially the necrotic region (Figure 6A).[5,23] As shown in Supporting Information S14, this information is now available in multiple slices where similar observations can be made and the full tumor can now be characterized. ROIs in the tumor core, the enhancing region, and contralateral white matter region, all of around 20 pixels in size, were defined in the coregistered contrast-enhanced T$_1$-weighted image for additional analysis. In the contrast-enhancing region the +3.5-ppm CEST contrast was significantly elevated with $(4.2 \pm 0.1)\%$ compared to contralateral white matter $(2.6 \pm 0.1)\%$ (mean and standard error). NOE CEST was almost unchanged with $(5.8 \pm 0.2)\%$ in the contrast-enhancing region compared to $(6.0 \pm 0.1)\%$ in the contralateral white matter. In the tumor core, the +3.5-ppm CEST contrast was slightly elevated compared to contralateral white matter with $(3.1 \pm 0.1)\%$ effect whereas the NOE CEST effect was significantly lower with $(4.3 \pm 0.2)\%$. Fitted CEST effects in all ROIs and for all contrasts are provided in Supporting Information Figure S13.

4 | DISCUSSION

The aim of the present work was to investigate whether the spectrally selective CEST effects, which have been observed and isolated at UHF, can also be obtained at clinical field strengths with a 3D method in a clinically justifiable time. Here, we demonstrate that this goal can be achieved by utilizing a fast 3D snapshot readout and strategically selected dense sampling of the Z-spectrum.

Because of the lower frequency separation at 3T, the CEST peak isolation is more difficult in comparison to UHF. However, a low-power saturation scheme in association with high-spectral-resolution sampling of the Z-spectrum allowed for discerning CEST effects when using a multistage Lorentzian fitting of the acquired signals. Using this approach, both amide CEST and NOE-CEST could be isolated and showed similar contrast in healthy volunteers and a tumor patient as reported previously at higher field strengths.[4,5,23,32]

4.1 | CEST contrasts at 3T

The amide-CEST effects reported here are difficult to compare to the well-established amide-proton transfer-weighted (APTw) scans performed at 3T, given that APTw experiments use high-power pulses and thus have a higher labeling and stronger weighting of faster exchanging protons. Despite that, the principle result of increased amide CEST effect in the tumor area[30] were also observed by the present spectrally selective low-power approach. Still, the tumor contrast in the isolated amide CEST signal was not as strong as in APTw imaging, and gray matter and tumor regions were also similar in intensity, which is in agreement with previous observations at UHF.[5] Thus, it remains to be investigated whether the isolated amide CEST gives a clinical benefit over APTw MRI at 3T.

The isolated NOE-CEST contrast, on the other hand, appeared to be aided by using the low-power approach compared to previous work at 3T. Heo et al[30] used a higher
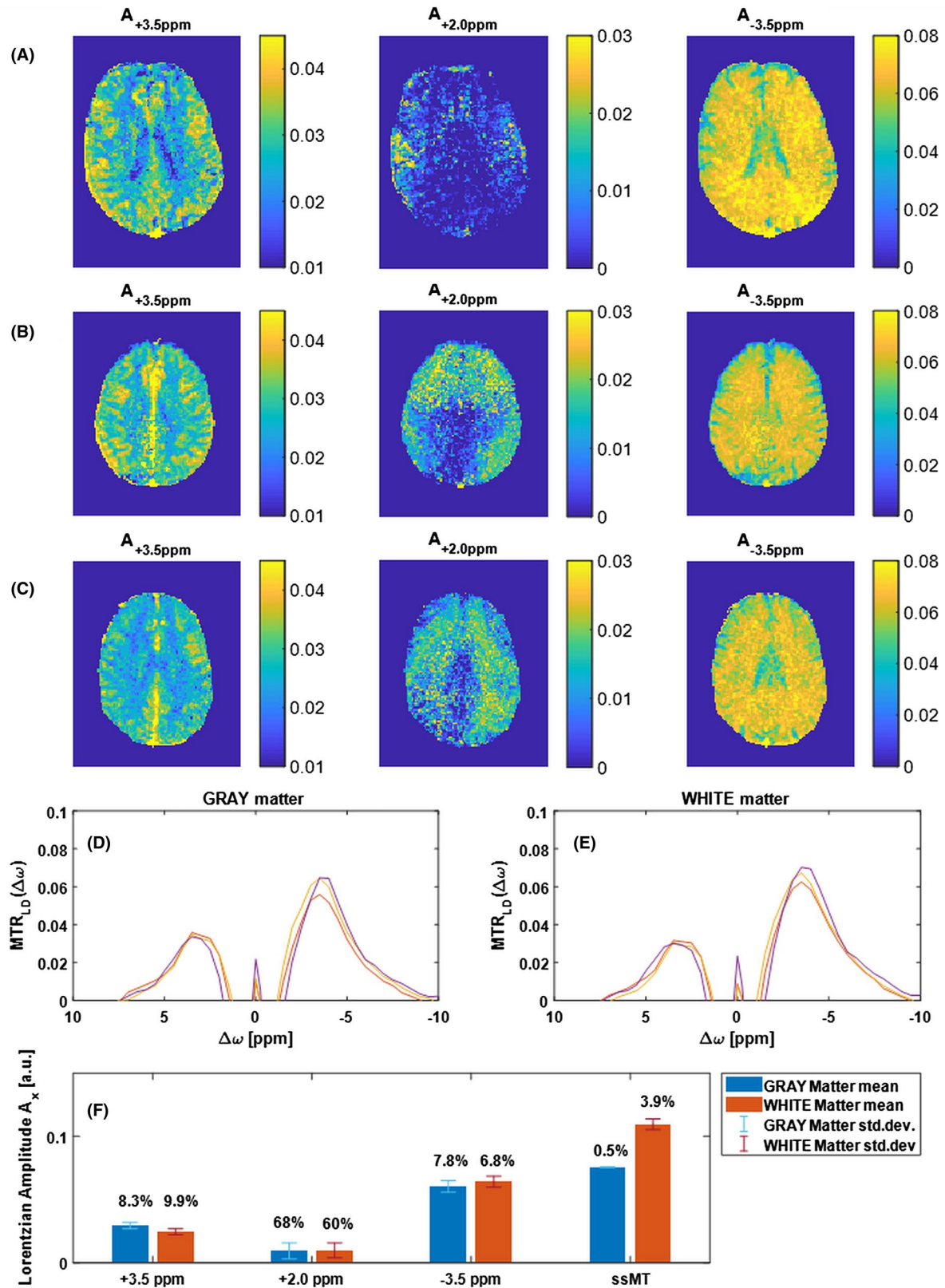
FIGURE 4 Reproducibility in 3 healthy subjects. (A–C) Isolated CEST effects obtained from 3-pool Lorentzian fitting of the MTR_{LD} spectrum (Equations 6 and 7). Whole-brain images are provided in Supporting Information Figure S12. The +2.0-ppm signal is strongly influenced by direct water saturation and residual off-resonance effects. (D,E) Mean MTR_{LD} spectra in gray and white matter segments. (F) Mean and standard deviation across subjects of fitted CEST effects in gray and white matter segments of a single slice. Slices were selected to have similar gray and white matter segments for each subject. Gray matter and white matter signals are clearly distinguishable for the +3.5-ppm, –3.5-ppm, and ssMT pools, with coefficient of variation for each pool and each ROI printed above each bar. MTR_{LD} spectra and fitted pool amplitudes are expressed in arbitrary units

power where the NOE is suppressed and an effect strength of only around 2% in white matter is reported, compared to our average effect strength of 6%. Shen et al[38] used similar saturation power to the current study, but longer saturation time and single-slice measurements. The NOE images obtained in our study had better quality in terms of SNR and resolution, as well as stronger NOE effect isolated by Lorentzian fitting.

A similar low-power, high-spectral-resolution protocol was recently applied to brain tumors by Desmond et al.[31] and Mehrabian et al.[39,40] They reported an amide-CEST effect of 3.4% and NOE-CEST effect of 7.3% in white matter, comparable to our findings. In tumors, they found both effects to be decreased. Notably, their approaches were single-slice measurements with at least 4 averages resulting in scan times reaching up to 12 minutes. Compared to single-slice methods, the 3D snapshot CEST approach used in this study improves SNR and coverage. Additionally, denoising using PCA reduced the number of required averages (see Supporting Information Figure S10), thereby making volumetric coverage available in clinically feasible examination times.

The snapshot CEST readout used in this work has been adapted from its original implementation at 9.4T.[23,32] The readout was accelerated and centric spiral reordered, but still Cartesian, facilitating reconstruction at the scanner. The current implementation is a proof of concept demonstrating that

a fast 3D readout can be used to isolate even small effect sizes at clinical field strengths. The signal of the snapshot gradient echo readout will decay with the Look-Locker relaxation time influenced both by T_1 relaxation and by excitation. With the current readout length of 738 k-space lines in 2.9 seconds, the actual resolution of the CEST images was reduced by a factor of 1.5 because of blurring of the point spread function. The readout used in this study was chosen as a trade-off between volume coverage and actual resolution; details about this trade-off are described in previous work.[32] Blurring can be reduced with a shorter readout at the cost of reduced resolution or volume coverage.

To adjust for lower SNR available at 3T, the current implementation used larger voxels, reduced acceleration, and a higher FA. It is possible to gain additional signal by reducing the readout BW or increasing the slice thickness. Note, however, that denoising of Z-spectra by methods as simple as PCA could improve the robustness of modelling of small-amplitude CEST signals at 3T. After denoising, adequate signals from amides and NOEs emerged with comparable contrast to that obtained at UHF. Moreover, these signals were robustly altered in the presence of pathology.

The present snapshot CEST approach measured approximately 7 seconds per irradiation frequency offset, whereas 30 seconds per irradiation frequency offset were necessary in recent 3D APTw imaging approaches.[29] Note also that
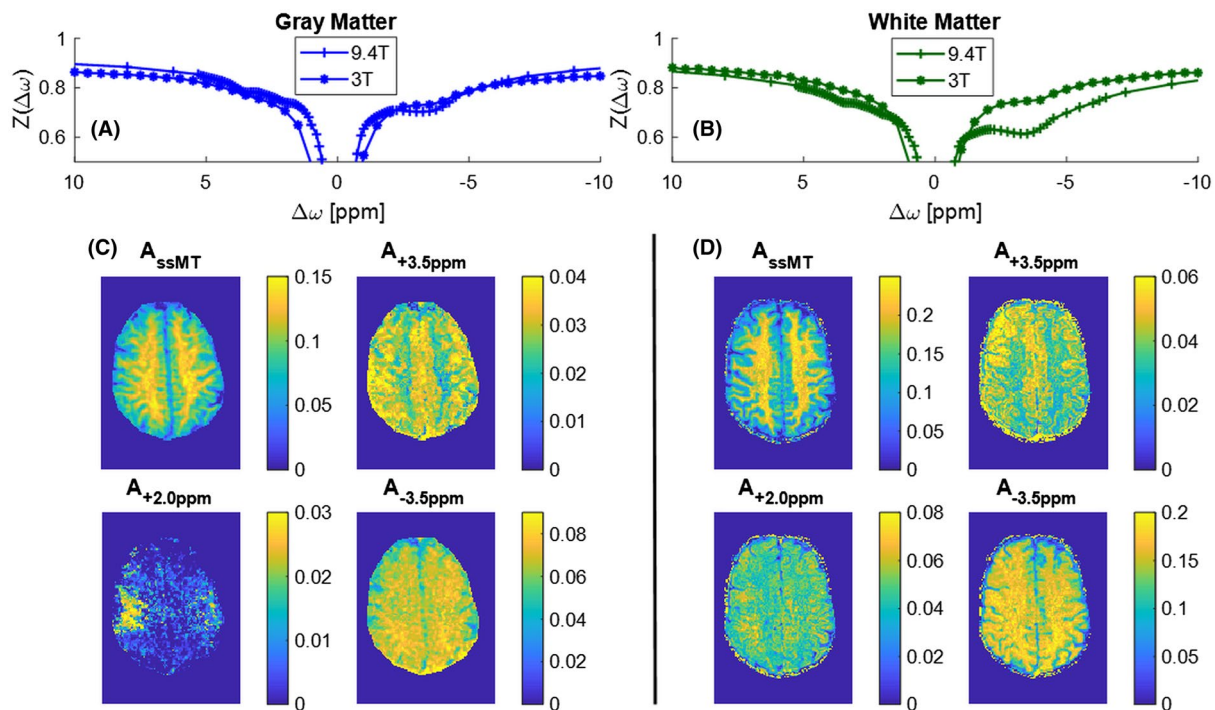
FIGURE 5 Comparison of spectrally selective CEST effects at 3 and 9.4T. (A,B) Z-spectra acquired at 3T show broader, coalesced effects compared to those acquired with similar saturation parameters at 9.4T. Still, fitted CEST contrast at 3T (C) shows similar distribution as observed at 9.4T (D), confirming spectral selectivity and indicating detectable effect size at +3.5 and −3.5 ppm. UHF strengths provide much higher SNR in comparison to 3T. Denoising 3T data allows for comparable contrast. Z-spectra and fitted pool amplitudes are expressed in arbitrary units

other saturation modules, such as APT-weighted, glucose-enhanced, or glutamate presaturation, are compatible with the snapshot 3D gradient echo readout.

4.2 | Saturation pulse duration and power level

In this study, we found that saturation times of 2.8 to 4 seconds, reflecting T_{sat} of $2.15 \cdot T_1$ to $3 \cdot T_1$ for gray matter at 3T, yielded similar CEST effect sizes. This observation agreed with pulsed CEST findings at 9.4T,[23] which showed that spectrally selective CEST effect sizes plateau at $T_{sat} > 1.7 \cdot T_1$, with reduced effects with less than 3 seconds of saturation.

The B_1 dispersion experiment in this study indicated that saturation pulses with powers in the range of 0.6 to 0.8 μT seem to be optimal for isolating CEST effects at +3.5 and –3.5 ppm. Higher B_1 powers may have more exchange weighting, but at the cost of spectral selectivity; this phenomenon was also observed in the human brain at 9.4T.[23] The B_1 inhomogeneity at 3T caused only 9% reduced CEST effect at the +3.5-ppm resonance and was only observed in the frontal brain regions (see Supporting Information Figure S12). Although no B_1 correction was performed for the 3T data in this study, it can be implemented at the cost of scan time because of the need for repeated measurements.[33]

Here, we used short Gaussian shaped pulses with 180° effective FA, which was reported to yield more CEST contrast.[37] However, short saturation pulses may not be optimal

for isolation of the +2.0-ppm signal. Maps of isolated CEST contrasts shown in Figure 4 indicate that the fitted +2.0-ppm resonance was influenced by residual B_0 inhomogeneity. Removing the +2.0-ppm signal from the MTR_{LD} fit resulted in these spillover effects appearing in the +3.5-ppm fitted contrast (see Supporting Information Figure S11). With a 3-pool model, the gray matter/white matter contrast in the +3.5-ppm CEST effect was more stable, but a trade-off was observed between fitting of the +3.5- and +2.0-ppm resonances, indicating that these effects overlapped using the current saturation scheme. The approach of Desmond et al.[31] used longer pulse durations and more-dense frequency sampling between ±0.5 and ±6 ppm, which allowed for better isolated amine contrast at +2.0 ppm than that obtained in the present study; such an approach could easily be applied with the 3D snapshot CEST readout. However, longer pulses might also lead to lower labeling as a narrower BW of CEST frequencies is labeled.[41,42] An adiabatic off-resonant spin lock pulse[43] with low direct saturation may also be of interest at lower field strengths for investigating resonances near water.

4.3 | Fit model

In this study, we used a 2-stage fitting approach for improved separation of CEST effects from direct water saturation and broad semisolid MT effects. This approach, which previously yielded spectrally selective CEST effects at 9.4T in mice[24] and humans,[23] also resulted in stronger contrast at 3T compared to 3-point fitting.[38] Measurement of far off-resonant
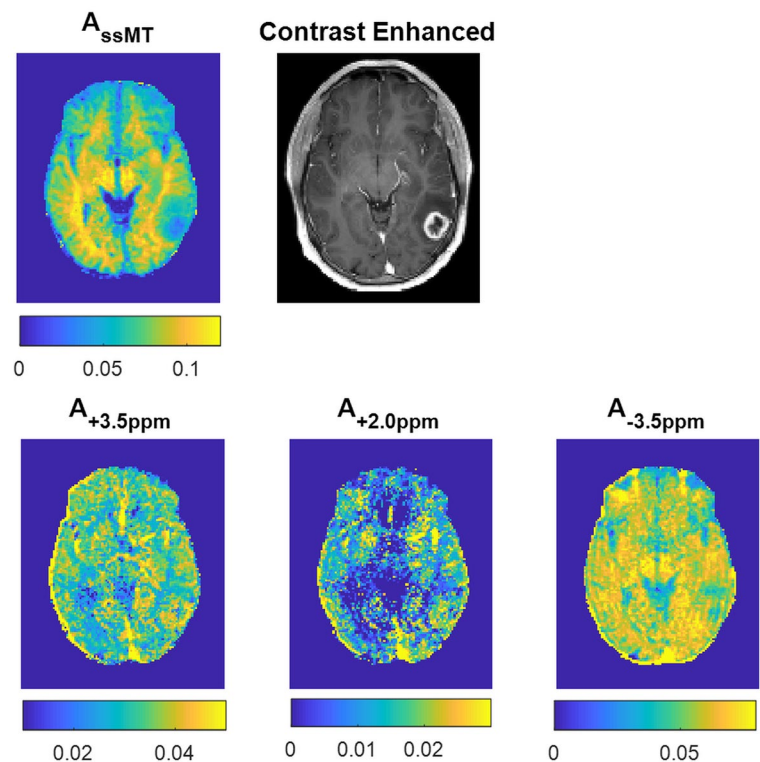
FIGURE 6 Isolated CEST effects in a patient with a brain tumor for a single slice. Images from surrounding slices are provided in Supporting Information Figure S14. Postcontrast T_1-weighted images show gadolinium ring enhancement, which coincides with hyperintensity at +3.5 ppm and isointensity at –3.5 ppm, and T_1 hypointensity corresponding to reduced signal in ssMT and –3.5-ppm CEST maps. All pool sizes are expressed in arbitrary units

frequency offsets beyond ± 6 ppm in particular facilitated the estimation of the ssMT contribution. Direct multi-Lorentzian fitting has also been applied in 3T low-power experiments,[31,40] where the ssMT contribution was modeled as a constant offset in the Z-spectrum between ± 6 ppm. The approach used in the present study allowed for asymmetric ssMT contributions, which is important especially for the separation of ssMT and NOE-CEST contributions.

4.4 | Outlook and clinical translation

It has been shown that the downfield amide proton signal is sensitive to pH, whereas the upfield NOE signal is pH-insensitive[44] and may be related to protein content[25] and protein denaturation[7] in brain tumors. Providing 3D coverage in less than 7 minutes of additional scan time, the snapshot CEST approach presented here can facilitate clinical translation of endogenous protein CEST contrast at 3T. With the addition of T_1 mapping, relaxation compensation[5] and downfield NOE suppression[6] analysis can be readily achieved.

5 | CONCLUSION

We have demonstrated feasibility of spectrally selective CEST imaging of NOE and amide effects at clinical field strength using a fast 3D snapshot CEST sequence, enabling full Z-spectrum sampling with volumetric coverage in a clinical time frame. Using an optimized saturation scheme with low B_1 power and high spectral resolution, combined with volumetric coverage and denoising, this approach allows for robust post-processing and reproducible isolated amide- and NOE-CEST contrasts in vivo. These methods provide similar gray matter/white matter contrast at 3T as can be obtained at 9.4T in healthy volunteers as well as in a tumor patient. Resonances closer to water visible at UHF strengths could not yet be robustly isolated at 3T using the current low-power approach.

ORCID

Anagha Deshmane http://orcid.org/0000-0003-0697-0895
Moritz Zaiss https://orcid.org/0000-0001-9780-3616

REFERENCES

1. Forsen S, Hoffman RA. Study of moderately rapid chemical exchange reactions by means of nuclear magnetic double resonance. *J Chem Phys*. 1963;39:2892–2901.
2. Ward K, Aletras A, Balaban R. A new class of contrast agents for MRI based on proton chemical exchange dependent saturation transfer (CEST). *J Magn Reson*. 2000;143:79–87.
3. Zhou J, Payen JF, Wilson DA, Traystman RJ, van Zijl P. Using the amide proton signals of intracellular proteins and peptides to detect pH effects in MRI. *Nat Med*. 2003;9:1085–1090.
4. Jones CK, Huang A, Xu J, et al. Nuclear Overhauser enhancement (NOE) imaging in the human brain at 7T. *NeuroImage*. 2013;77:114–124.
5. Zaiss M, Windschuh J, Paech D, et al. Relaxation-compensated CEST-MRI of the human brain at 7T: unbiased insight into NOE and amide signal changes in human glioblastoma. *NeuroImage*. 2015;112:180–188.
6. Zaiss M, Windschuh J, Goerke S, et al. Downfield-NOE-suppressed amide-CEST-MRI at 7 Tesla provides a unique contrast in human glioblastoma. *Magn Reson Med*. 2017;77:196–208.
7. Zaiss M, Kunz P, Goerke S, Radbruch A, Bachert P. MR imaging of protein folding in vitro employing Nuclear-Overhauser-mediated saturation transfer. *NMR Biomed*. 2013;26:1815–1822.
8. Goerke S, Zaiss M, Kunz P, et al. Signature of protein unfolding in chemical exchange saturation transfer imaging. *NMR Biomed*. 2015;28:906–913.
9. Goerke S, Milde KS, Bukowiecki R, et al. Aggregation-induced changes in the chemical exchange saturation transfer (CEST) signals of proteins. *NMR Biomed*. 2017;30:e3665.
10. Kogan F, Haris M, Singh A, et al. Method for high-resolution imaging of creatine in vivo using chemical exchange saturation transfer. *Magn Reson Med*. 2014;71:164–172.
11. Rerich E, Zaiss M, Korzowski A, Ladd ME, Bachert P. Relaxation-compensated CEST-MRI at 7 T for mapping of creatine content and pH—preliminary application in human muscle tissue in vivo. *NMR Biomed*. 2015;28:1402–1412.
12. Cai K, Haris M, Singh A, et al. Magnetic resonance imaging of glutamate. *Nat Med*. 2012;18:302–306.
13. Haris M, Nath K, Cai K, et al. Imaging of glutamate neurotransmitter alterations in Alzheimer's disease. *NMR Biomed*. 2013;26:386–391.
14. Aime S, Calabi L, Biondi L, et al. Iopamidol: Exploring the potential use of a well-established x-ray contrast agent for MRI. *Magn Reson Med*. 2005;53:830–834.
15. Longo DL, Busato A, Lanzardo S, Antico F, Aime S. Imaging the pH evolution of an acute kidney injury model by means of iopamidol, a MRI-CEST pH-responsive contrast agent. *Magn Reson Med*. 2013;70:859–864.
16. Jones KM, Randtke EA, Howison CM, et al. Measuring extracellular pH in a lung fibrosis model with acidoCEST MRI. *Mol Imaging Biol*. 2015;17:177–184.
17. Chan KW, McMahon MT, Kato Y, et al. Natural D-glucose as a biodegradable MRI contrast agent for detecting cancer. *Magn Reson Med*. 2012;68:1764–1773.
18. Walker-Samuel S, Ramasawmy R, Torrealdea F, et al. In vivo imaging of glucose uptake and metabolism in tumors. *Nat Med*. 2013;19:1067–1072.

19. Xu X, Yadav NN, Knutsson L, et al. Dynamic glucose-enhanced (DGE) MRI: translation to human scanning and first results in glioma patients. *Tomography*. 2015;1:105–114.

20. Schuenke P, Koehler C, Korzowski A, et al. Adiabatically prepared spin-lock approach for T1ρ-based dynamic glucose enhanced MRI at ultrahigh fields. *Magn Reson Med*. 2017;78:215–225.

21. Nasrallah FA, Pagès G, Kuchel PW, Golay X, Chuang KH. Imaging brain deoxyglucose uptake and metabolism by gluco-CEST MRI. *J Cereb Blood Flow Metab*. 2013;33:1270–1278.

22. Rivlin M, Tsarfaty I, Navon G. Functional molecular imaging of tumors by chemical exchange saturation transfer MRI of 3-O-Methyl-D-glucose. *Magn Reson Med*. 2014;72:1375–1380.

23. Zaiss M, Schuppert M, Deshmane A, et al. Chemical exchange saturation transfer MRI contrast in the human brain at 9.4 T. *NeuroImage*. 2018;179:144–155.

24. Cai K, Singh A, Poptani H, et al. CEST signal at 2 ppm (CEST@2 ppm) from Z -spectral fitting correlates with creatine distribution in brain tumor. *NMR Biomed*. 2014;28:1–8.

25. Paech D, Burth S, Windschuh J, et al. Nuclear overhauser enhancement imaging of glioblastoma at 7 Tesla: region specific correlation with apparent diffusion coefficient and histology. *PLoS ONE*. 2015;10:1–16.

26. Meissner JE, Regnery S, Korozowski A, et al. NOE-mediated CEST imaging of glioma at 7 Tesla aids early response evaluation of patients undergoing radio-chemotherapy. In: Proceedings of the Joint Annual Meeting ISMRM-ESMRMB, Paris, France, 2018. p. 408.

27. Zhu H, Jones CK, van Zijl PC, Barker PB, Zhou J. Fast 3D chemical exchange saturation transfer (CEST) imaging of the human brain. *Magn Reson Med*. 2010;64:638–644.

28. Togao O, Yoshiura T, Keupp J, et al. Amide proton transfer imaging of adult diffuse gliomas: correlation with histopathological grades. *Neuro Oncol*. 2014;16:441–448.

29. Togao O, Keupp J, Hiwatashi A, et al. Amide proton transfer imaging of brain tumors using a self-corrected 3D fast spin-echo dixon method: comparison with separate B_0 correction. *Magn Reson Med*. 2017;77:2272–2279.

30. Heo HY, Zhang Y, Jiang S, Lee DH, Zhou J. Quantitative assessment of amide proton transfer (APT) and nuclear overhauser enhancement (NOE) imaging with extrapolated semisolid magnetization transfer reference (EMR) signals: II. Comparison of three EMR models and application to human brain glioma at. *Magn Reson Med*. 2016;75:1630–1639.

31. Desmond KL, Mehrabian H, Chavez S, et al. Chemical exchange saturation transfer for predicting response to stereotactic radiosurgery in human brain metastasis. *Magn Reson Med*. 2017;78:1110–1120.

32. Zaiss M, Ehses P, Scheffler K. Snapshot-CEST: optimizing spiral-centric-reordered gradient echo acquisition for fast and robust 3D CEST MRI at 9.4 T. *NMR Biomed*. 2018;31:e3879.

33. Windschuh J, Zaiss M, Meissner JE, et al. Correction of B1-inhomogeneities for relaxation-compensated CEST imaging at 7T. *NMR Biomed*. 2015;28:529–537.

34. Griswold MA, Jakob PM, Heidemann RM, et al. Generalized autocalibrating partially parallel acquisitions (GRAPPA). *Magn Reson Med*. 2002;47:1202–1210. https://doi.org/10.1002/mrm.10171

35. Walsh D, Gmitro A, Marcellin M. Adaptive reconstruction of phased array MR imagery. *Magn Reson Med*. 2000;43:682–690.

36. Cox RW, Hyde JS. Software tools for analysis and visualization of fMRI data. *NMR Biomed*. 1997;10:171–178.

37. Zu Z, Li K, Janve VA, Does MD, Gochberg DF. Optimizing pulsed-chemical exchange saturation transfer imaging sequences. *Magn Reson Med*. 2011;66:1100–1108.

38. Shen Y, Xiao G, Shen Z, et al. Imaging of nuclear Overhauser enhancement at 7 and 3 T. *NMR Biomed*. 2017;30:e3735.

39. Mehrabian H, Lam WW, Myrehaug S, Sahgal A, Stanisz GJ. Glioblastoma (GBM) effects on quantitative MRI of contralateral normal appearing white matter. *J Neurooncol*. 2018;139:97–106.

40. Mehrabian H, Myrehaug S, Soliman H, Sahgal A, Stanisz GJ. Evaluation of glioblastoma response to therapy with chemical exchange saturation transfer. *Int J Radiat Oncol*. 2018;101:713–723.

41. van Zijl P, Lam WW, Xu J. Knutsson L, Stanisz GJ. Magnetization transfer contrast and chemical exchange saturation transfer MRI. Features and analysis of the field-dependent saturation spectrum. *NeuroImage*. 2018;168:222–241.

42. Goerke S, Breitling J, Zaiss M, et al. Dual-frequency irradiation CEST-MRI of endogenous bulk mobile proteins. *NMR Biomed*. 2018;31:e3920.

43. Herz K, Gandhi C, Schuppert M, Deshmane A, Scheffler K, Zaiss M. CEST imaging at 9.4 T using adjusted adiabatic spin-lock pulses for on- and off-resonant T1ρ-dominated Z-spectrum acquisition. *Magn Reson Med*. 2018 Sep 8. doi: https://doi.org/10.1002/mrm.27380.

44. Jin T, Wang P, Zong X, Kim SG. MR imaging of the amide-proton transfer effect and the pH-insensitive nuclear overhauser effect at 9.4 T. *Magn Reson Med*. 2013;69:760–770.

SUPPORTING INFORMATION

Additional supporting information may be found online in the Supporting Information section at the end of the article.

FIGURE S1 Simulated Z-spectra in gray matter and white matter under low-power pulsed and continuous wave (CW) saturation

FIGURE S2 Residual of 4 fit models to simulated continuous wave saturation at equivalent power to Supporting Information Figure S1, zoomed to show points near 0 ppm (rows 1–4) and far off-resonance (rows 5–8)

FIGURE S3 Residual of four 2-pool fit models to simulated pulsed saturation schemes, zoomed to show points near 0 ppm (rows 1–4) and far off-resonance (rows 5–8). Total saturation time is kept constant at 4 seconds, and pulse amplitude and duration are varied to achieve approximately 180° rotation

FIGURE S4 In vivo MTR_{LD} using four 2-pool models to fit the background (DS + MT) of Z-spectra measured using pulsed saturation schemes, zoomed to show points near 0 ppm (rows 1–4) and far off-resonance (rows 5–8)

FIGURE S5 In vivo MTR_{LD} using 2-pool Lorentzian and super-Lorentzian with BW model to fit the background (water + ssMT) of Z-spectra measured using pulsed saturation (100 Gaussian-shaped pulses, 0.6 μT, t_p = 20 ms, 50 %

duty cycle), zoomed to show points near 0 ppm (rows 1–4) and far off-resonance (rows 5–8)

FIGURE S6 Simulated 2-pool Z-spectra of white matter for 0.6-μT continuous wave saturation using the Henkelman model with a centered super-Lorentzian MT line shape (solid black line) and shifted super-Lorentzian MT lineshape (red dashed line). In addition to the background, a sharp peak at the MT resonance shift of –2.34 ppm is visible in the shifted line shape. This peak can be removed by interpolation of the MT line shape within an interval of ±1 ppm around the MT resonance frequency (blue solid line), but the resulting line shape depends on the arbitrarily chosen interpolation interval (blue, pink, and yellow dashed lines)

FIGURE S7 PCA of Z-spectra. (a) First 4 principle components exhibiting spectral features near 0 ppm. (b) All principle components, exhibiting broad CEST spectral features between ±5 ppm (components 5–20) and noise-like features (components 20–53)

FIGURE S8 Projection of data of a single slice from a healthy subject onto principle components. The first few components contain anatomical and experimentally relevant information, whereas the remaining components contribute noise

FIGURE S9 Eigenvalues of principle components of measured Z-spectra in 5 healthy volunteers. The stars denote the optimal number of components based on Malinowski's empirical indicator function

FIGURE S10 Effect of denoising of Z-spectra on CEST contrast when retaining 42, 36, 27, 14, 11, 9, and 6 of 53 components compared to averaging of repeated measurements. MTR_{LD} is expressed in arbitrary units

FIGURE S11 Including the +2.0-ppm pool in the MTR_{LD} analysis improves the stability of the fit at +3.5 ppm. Using a 2-pool fit, the +3.5-ppm fitted resonance is influenced by direct water saturation and residual B_0 errors

FIGURE S12 Whole-brain fitted CEST contrasts from which single slice images in Figure 4a to 4c were extracted

FIGURE S13 Mean and standard deviation of fitted Lorentzian pool sizes in single-slice ROIs in the brain tumor patient

FIGURE S14 Fitted background (water, DS, and ssMT) and CEST contrasts in several slices covering the tumor. Gadolinium contrast-enhanced images are provided for reference

TABLE S1 Pulsed and continuous wave power equivalent (CWPE) protocols used in Bloch simulation Abbreviations: t_p, pulse duration; DC, duty cycle

TABLE S2 Gray matter and white matter parameters employed in Bloch simulation Values are taken from a previous work.[1] Δω, frequency offset; ppm, parts per million; f, pool fraction; k, exchange rate

TABLE S3 Boundary and initial conditions of the 2-pool Lorentzian model used for background fitting

TABLE S4 Boundary and initial conditions of the 2-pool super-Lorentzian model used for background fitting Pool A refers to water, pool C refers to the macromolecular pool

TABLE S5 Boundary and initial conditions of the 3-pool Lorentzian model used for CEST pool fitting of $MTR_{LD,net}$

TABLE S6 Frequency offsets used in multistage fitting